

# Polarization of thermal bremsstrahlung emission due to electron pressure anisotropy

S. V. Komarov<sup>1,2\*</sup>, I. I. Khabibullin<sup>1,2</sup>, E. M. Churazov<sup>1,2</sup> and A. A. Schekochihin<sup>3,4</sup>

<sup>1</sup>Max Planck Institute for Astrophysics, Karl-Schwarzschild-Strasse 1, 85741 Garching, Germany

<sup>2</sup>Space Research Institute (IKI), Profsovnaya 84/32, Moscow 117997, Russia

<sup>3</sup>The Rudolf Peierls Centre for Theoretical Physics, University of Oxford, 1 Keble Road, Oxford OX1 3NP, United Kingdom

<sup>4</sup>Merton College, Oxford OX1 4JD, United Kingdom

11 March 2021

## ABSTRACT

Astrophysical plasmas are typically magnetized, with the Larmor radii of the charged particles many orders of magnitude smaller than their collisional mean free paths. The fundamental properties of such plasmas, e.g., conduction and viscosity, may depend on the instabilities driven by the anisotropy of the particle distribution functions and operating at scales comparable to the Larmor scales. We discuss a possibility that the pressure anisotropy of thermal electrons could produce polarization of thermal bremsstrahlung emission. In particular, we consider coherent large-scale motions in galaxy clusters to estimate the level of anisotropy driven by stretching of the magnetic-field lines by plasma flow and by heat fluxes associated with thermal gradients. Our estimate of the degree of polarization is  $\sim 0.1\%$  at energies  $\gtrsim kT$ . While this value is too low for the forthcoming generation of X-ray polarimeters, it is potentially an important proxy for the processes taking place at extremely small scales, which are impossible to resolve spatially. The absence of the effect at the predicted level may set a lower limit on the electron collisionality in the ICM. At the same time, the small value of the effect implies that it does not preclude the use of clusters as (unpolarized) calibration sources for X-ray polarimeters at this level of accuracy.

**Key words:** ICM, plasmas, magnetic field, polarization

## 1 INTRODUCTION

For the electrons in a hot tenuous astrophysical plasma, the equilibration time scale due to Coulomb collisions is often sufficiently long compared to other characteristic time scales to allow for deviations from thermal equilibrium manifested by anisotropies or non-thermal tails. The latter typically require a mechanism to accelerate a fraction of particles to high energies, e.g., magnetic reconnection or diffusive shock acceleration (Krymskii 1977; Axford et al. 1977; Blandford & Ostriker 1978; Bell 1978). Anisotropies, on the other hand, are commonly associated with the presence of a magnetic field.

In many astrophysical plasmas, magnetic fields are strong enough to force a charged particle to orbit around a field line with the Larmor radius many orders of magnitude smaller than the particle’s collisional mean free path. If the magnetic field is not constant in time, adiabatic invariance compels the perpendicular and parallel components of the particle’s velocity to adjust to the field magnitude in differ-

ent ways, thus producing pressure anisotropy (Chew et al. 1956; Kulsrud 1964). A heat flux along the field lines also contributes to anisotropy. Above a certain threshold, pressure anisotropies trigger kinetic microinstabilities, e.g., firehose and mirror (Chandrasekhar et al. 1958; Parker 1958; Hasegawa 1969), which are believed to hold the anisotropy at a marginal level by increasing the effective collision rate via scattering off magnetic perturbations and magnetic trapping (for observational evidence in the solar wind, see Kasper et al. 2002; Hellinger et al. 2006; Bale et al. 2009; for theoretical discussion, see, e.g., Kunz et al. 2014; Melville et al. 2015 and references therein).

Temporal changes of magnetic-field strength may be caused by random turbulent motions or by a specific ordered plasma flow, e.g., a flow past a cold dense cloud of gas in “cold fronts” in the ICM (see, e.g., Markevitch & Vikhlinin 2007, for a review) or a shear flow in accretion disks (Sharma et al. 2006). Cold fronts also manifest sharp temperature gradients at the interface between the cold cloud and the hot ambient plasma. In a hot rarefied plasma, the electron temperature anisotropy generated by both the magnetic-field evolution and heat fluxes leaves an imprint in

\* E-mail: komarov@mpa-garching.mpg.de

the form of polarization of bremsstrahlung emission (for an example in solar flares, see, e.g., Haug 1972). If a flow orients the magnetic field in some preferential direction, the polarization does not cancel out and potentially can be observed by X-ray polarimeters.

In this paper, we examine the possible magnitude and detectability of electron pressure anisotropy in galaxy clusters. We start by describing the theoretical framework for the problem at hand. Generation of pressure anisotropies in a plasma with evolving magnetic fields and temperature gradients is discussed in Section 2.1. In Section 2.2, we derive the polarization of bremsstrahlung emission for a given anisotropic bi-Maxwellian electron distribution. Then we proceed with application of our theory to cold fronts and shocks in the ICM with the help of analytical models and numerical MHD simulations (Section 3). The effects are weak, of order 0.1%, but they produce a characteristic pattern and may provide constraints on the pressure anisotropy and electron collisionality in the ICM. We briefly discuss the role of the effects for observations of galaxy clusters with future X-ray calorimeters in Section 4. Finally, we summarize our findings in Section 5.

## 2 THEORETICAL FRAMEWORK

### 2.1 Generation of pressure anisotropies in a weakly collisional plasma

In an astrophysical plasma, the Larmor radii  $\rho_s$  of all particle species are typically much smaller than their collisional mean free paths  $\lambda_s$ ; equivalently, their collision frequencies  $\nu_s$  are much smaller than the Larmor frequencies  $\Omega_s$  ( $s = i, e$ , with  $e$  the electrons,  $i$  the ions). If the magnetic-field strength  $B$  changes slowly,  $\gamma = B^{-1}dB/dt$ , each particle conserves its first adiabatic invariant  $\mu = v_{\perp s}^2/2B \propto p_{\perp s}/B$ , which is the magnetic moment of the particle, where  $v_{\perp s}$  is the component of the particle's velocity perpendicular to the field line,  $p_{\perp s}$  is the perpendicular pressure. To demonstrate how pressure anisotropy is driven and sustained by evolving magnetic fields in an incompressible plasma with no heat flux, we express the assumption that  $\mu$  is conserved but for rare occasional collision as

$$\frac{1}{p_{\perp s}} \frac{dp_{\perp s}}{dt} \sim \frac{1}{B} \frac{dB}{dt} - \nu_s \frac{p_{\perp s} - p_{\parallel s}}{p_{\perp s}}, \quad (1)$$

where  $p_{\parallel s}$  is the parallel pressure, and the last term corresponds to isotropization of pressure by collisions. If  $\gamma \ll \nu_s$ , the pressure anisotropy  $\Delta_s$  can be estimated from the balance between the collisional relaxation and the rate of change of the magnetic field:

$$\Delta_s \equiv \frac{p_{\perp s} - p_{\parallel s}}{p_s} \sim \frac{1}{\nu_s} \frac{1}{B} \frac{dB}{dt} = \frac{\gamma}{\nu_s}. \quad (2)$$

It is clear from this estimate that the electron anisotropy is  $\nu_e/\nu_i \sim (m_i/m_e)^{1/2} \approx 40$  times weaker than that of the ions (if the electron and ion temperatures are equal).

The more general form of  $\Delta_s$  taking into account the evolution of the parallel pressure can be obtained from the so-called CGL equations (Chew et al. 1956) with collisions retained, which are derived by taking second moments of the kinetic magnetohydrodynamics equations (KMHD).

The KMHD equations arise after averaging the full kinetic equation over the gyroangle. The CGL equations read (Schekochihin et al. 2010)

$$p_{\perp s} \frac{d}{dt} \ln \frac{p_{\perp s}}{n_s B} = \nabla \cdot (q_{\perp s} \mathbf{b}) - q_{\perp s} \nabla \cdot \mathbf{b} - \nu_s (p_{\perp s} - p_{\parallel s}), \quad (3)$$

$$p_{\parallel s} \frac{d}{dt} \ln \frac{p_{\parallel s} B^2}{n_s^3} = \nabla \cdot (q_{\parallel s} \mathbf{b}) + 2q_{\perp s} \nabla \cdot \mathbf{b} - 2\nu_s (p_{\parallel s} - p_{\perp s}), \quad (4)$$

where  $d/dt = \partial/\partial t + \mathbf{u}_s \cdot \nabla$  is the convective derivative associated with species  $s$  ( $\mathbf{u}_s$  is the plasma flow velocity),  $\mathbf{b}$  is the unit vector in the direction of the magnetic field,  $n_s$  the number densities,

$$p_{\perp s} = \int d^3 \mathbf{w} \frac{m_s w_{\perp}^2}{2} f_s, \quad (5)$$

$$p_{\parallel s} = \int d^3 \mathbf{w} m_s w_{\parallel}^2 f_s \quad (6)$$

are the perpendicular and parallel pressures,

$$q_{\perp s} = \int d^3 \mathbf{w} \frac{m_s w_{\perp}^2}{2} w_{\parallel} f_s, \quad (7)$$

$$q_{\parallel s} = \int d^3 \mathbf{w} m_s w_{\parallel}^3 f_s, \quad (8)$$

$q_{\perp s}$  and  $q_{\parallel s}$  are heat fluxes (the parallel flux of the ‘‘perpendicular internal energy’’ and the parallel flux of the ‘‘parallel internal energy’’, respectively),  $\mathbf{w}$  the thermal component of a particle's velocity,  $f_s$  the distribution functions of the particles. Subtracting equation (4) from equation (3), we get an evolution equation for the pressure anisotropy:

$$\frac{d}{dt} (p_{\perp s} - p_{\parallel s}) = (p_{\perp s} + 2p_{\parallel s}) \frac{1}{B} \frac{dB}{dt} + (p_{\perp s} - 3p_{\parallel s}) \frac{1}{n_s} \frac{dn_s}{dt} - \nabla \cdot [(q_{\perp s} - q_{\parallel s}) \mathbf{b}] - 3q_{\perp s} \nabla \cdot \mathbf{b} - 3\nu_s (p_{\perp s} - p_{\parallel s}). \quad (9)$$

Assuming that collisions are fast compared to the fluid motions, the pressure anisotropy is then small,  $p_{\parallel s} - p_{\perp s} \ll p_{\perp s} \approx p_{\parallel s} \approx p_s$ , the collisional heat fluxes are  $q_{\perp s} \approx (1/3)q_{\parallel s}$ , and the total heat flux along a field line  $q_s = q_{\perp s} + q_{\parallel s}/2 = (5/6)q_{\parallel s}$ . The value of the anisotropy is set by the balance between collisional relaxation and various driving terms:

$$\Delta_s \equiv \frac{p_{\perp s} - p_{\parallel s}}{p_s} \approx \frac{1}{\nu_s} \left[ \frac{1}{B} \frac{dB}{dt} - \frac{2}{3} \frac{1}{n_s} \frac{dn_s}{dt} + \frac{4\nabla \cdot (q_s \mathbf{b}) - 6q_s \nabla \cdot \mathbf{b}}{15p_s} \right]. \quad (10)$$

Thus, the pressure anisotropy is driven by changing magnetic-field strength, changing particle density, and by parallel heat fluxes.

It is useful to estimate the degree of anisotropy induced by different driving terms in equation (10). If we consider fluid motions with velocity  $u$  at scale  $L_u$ , variations of  $B$  at the scale of the velocity field  $L_B = L_u$ , and parallel temperature gradient  $\nabla_{\parallel} T_s \sim \delta T_s/L_T$  at scale  $L_T$ , we can evaluate the contribution  $\Delta_{B,n;s}$  of changing  $B$  and  $n$ , and the contribution  $\Delta_{T;s}$  of the heat fluxes, to the total anisotropy

as

$$\Delta_{B,n;s} \sim \frac{u}{v_{\text{th},s}} \frac{\lambda_s}{L_u}, \quad (11)$$

$$\Delta_{T;s} \sim \frac{\lambda_s^2}{L_T L_u} \frac{\delta T_s}{T_s}, \quad (12)$$

where we have used the expression for the heat flux  $q_s = -\kappa_s \nabla_{\parallel} T_s$  with thermal conductivity  $\kappa_s \sim n_s v_{\text{th},s} \lambda_s$ ,  $\lambda_s$  is the mean free path,  $v_{\text{th},s}$  the thermal speed. Assume that the flow velocity is nearly sonic,  $u \sim v_{\text{th},i}$ , and that the variations of temperature are of order unity,  $\delta T/T \sim 1$ . Then  $\Delta_T \sim \lambda^2/(L_u L_T)$  for both particle species, and  $\Delta_{B,n;s} \sim \lambda/L_u \times v_{\text{th},s}/v_{\text{th},i}$ . Hence, in our ordering, for the ions, the term linked to the magnetic-field changes  $\Delta_{B,n;i} \sim \lambda/L_u$  is dominant if  $L_T \gg \lambda$  (even in astrophysical systems with very sharp temperature gradients, e.g., cold fronts or buoyant bubbles of relativistic plasma in the ICM, the magnetic-field lines are typically stretched by the fluid flow in the direction perpendicular to the gradient (e.g., Komarov et al. 2014), thus significantly increasing the scale of temperature variation along the field lines). For the electrons,  $\Delta_{B,n;e} \sim 1/40 \times \lambda/L_u$ , and the two contributions can be of the same order ( $\Delta_{B,n;e} \sim \Delta_{T;e}$ ), depending on the properties of the flow and the orientation of the magnetic-field lines connecting the hot and cold regions of the plasma. Note that the total anisotropy is bounded from below by the firehose instability,  $\Delta_e + \Delta_i > -2/\beta$ , where  $\beta$  is the ratio of thermal to magnetic-energy densities. If the ion and electron anisotropies are small ( $\Delta_i, \Delta_e \ll 1$ ), the mirror instability also compels the total anisotropy to stay below the mirror marginal level,  $\Delta_e + \Delta_i \lesssim 1/\beta$ . Therefore, in regions of high plasma  $\beta$ , either  $\gamma (= B^{-1} dB/dt)$  or  $\nu_s$  is modified by the instabilities to keep the anisotropy between the marginal levels,  $-2/\beta < \Delta_e + \Delta_i < 1/\beta$  (e.g., Kunz et al. 2014; Melville et al. 2015). In Appendix A, we calculate the total anisotropy for the simulated cold fronts (Section 3) and mark the regions where firehose and mirror instabilities could develop. Because in our work the ion anisotropy is typically dominant, the two instabilities are regulated by the ions.

We are primarily interested in electron pressure anisotropy because of its possible observational imprint in the form of polarization of thermal bremsstrahlung. From the above estimates, it is clear that in the case of astrophysical systems with large temperature gradients, the driving term linked to heat fluxes must be taken into account along with the driving by the magnetic-field changes. We do this in detail for cold fronts in Section 3.

## 2.2 Polarization of thermal bremsstrahlung by electron anisotropy

Consider first the polarization of bremsstrahlung emission from an electron beam deflected by a single ion. At low energies (compared to the kinetic energy of an electron), photons produced by small-angle scattering of the electrons off the ion are polarized in the plane perpendicular to the electron beam due to the mainly perpendicular acceleration that slightly changes the direction of the electron velocity. At higher energies, when both the direction and magnitude of the electron velocity change significantly, polarization becomes dominated by the acceleration the electrons experi-

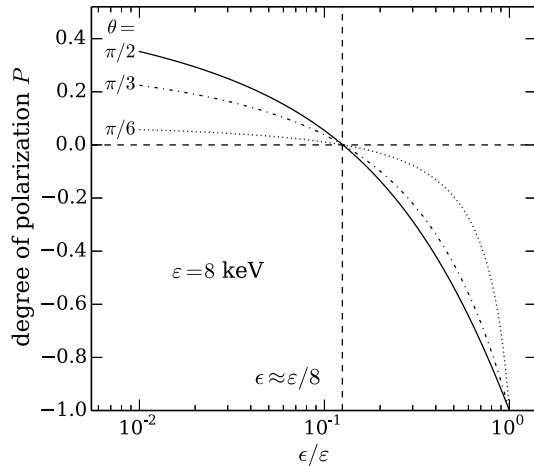


**Figure 1.** The degree of bremsstrahlung polarization  $P(\epsilon, \theta) = (d^2\sigma_{\perp} - d^2\sigma_{\parallel})/(d^2\sigma_{\perp} + d^2\sigma_{\parallel})$  from a beam of electrons of energy  $\epsilon = 8$  KeV as a function of the emitted photon's energy  $\epsilon$  and the angle  $\theta$  between the beam axis and the photon's momentum.

ence parallel to the beam. Below, we demonstrate that the latter regime is of first importance for our problem, because the degree of polarization is considerably larger at high energies in the case of thermal bremsstrahlung from a cloud of anisotropic electrons.

Bremsstrahlung emission from a beam of electrons of kinetic energy  $\epsilon$  is fully described by differential cross sections per unit solid angle and photon energy,  $d^2\sigma_{\perp}(\epsilon, \theta)$  and  $d^2\sigma_{\parallel}(\epsilon, \theta)$ , for the components perpendicular and parallel to the radiation plane (spanned by an emitted photon's and an initial electron's momenta). Here,  $d^2 = d/(d\epsilon d\Omega)$ ,  $\epsilon$  stands for the emitted photon's energy, and  $\theta$  for the angle between the emitted photon's momentum and the beam axis. We use the fully relativistic cross sections calculated by Gluckstern & Hull (1953) in the first Born approximation, which are appropriate for the problem at hand<sup>1</sup>. Because the formulae in the original paper by Gluckstern & Hull (1953), as well as those given later by Bai & Ramaty (1978), are both replete with typos, we provide the correct explicit expressions for the cross sections in Appendix B. The degree of polarization is  $P(\epsilon, \theta) = (d^2\sigma_{\perp} - d^2\sigma_{\parallel})/(d^2\sigma_{\perp} + d^2\sigma_{\parallel}) = d^2\sigma_1/d^2\sigma_0$ , where  $d^2\sigma_1$  is the differential cross section of the polarized emission,  $d^2\sigma_0$  of the total emission. Its dependence on the photon energy and direction with respect to the beam axis is illustrated in Fig. 1. The transition between the perpendicular and parallel polarization occurs at photon energy  $\epsilon \approx \epsilon_0/8$ . As noted before, the perpendicular polarization at low energies is produced by small-angle scattering of the electrons, while the parallel is the result of collisions that significantly change the electron energy.

Since the differential cross sections presented above are

<sup>1</sup> The limit of validity of this approximation is given by condition  $\epsilon'/m_e c^2 \gg (Z/137)^2$ , where  $Z$  is the charge of the scattering ion in atomic units,  $\epsilon'$  the energy of an outgoing electron (Gluckstern & Hull 1953). For  $Z = 1$ , the condition is satisfied for outgoing electrons at energies  $\epsilon' \gg 30$  eV.

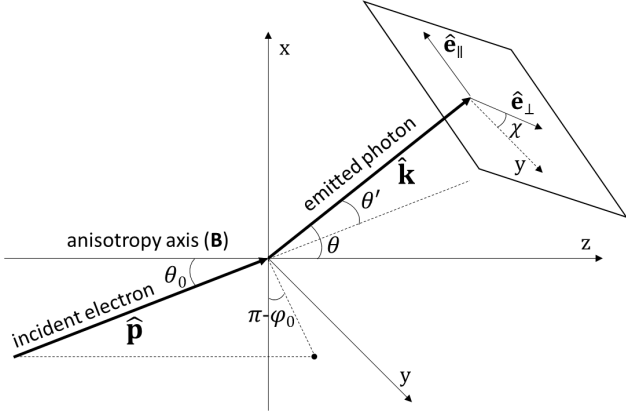


**Figure 2.** Geometry for the problem of the polarization of bremsstrahlung emission from a cloud of electrons.

essentially the “Green’s functions” of the bremsstrahlung emission, the total and polarized emission from a cloud of electrons can be found by integrating over the electron distribution function. Let us introduce a spherical coordinate system and assume that the electron distribution is axisymmetric with respect to the magnetic-field direction, taken to be the  $z$  axis. We denote the unit vector in the direction of the incoming electron  $\hat{\mathbf{p}} = (\sin \theta_0 \cos \phi_0, \sin \theta_0 \sin \phi_0, \cos \theta_0)$ , and the direction of the line of sight  $\hat{\mathbf{k}} = (\sin \theta, 0, \cos \theta)$  (choose  $\phi = 0$  without loss of generality because the resulting polarization pattern is also axisymmetric). The geometry of the vectors is illustrated in Fig. 2. The polarization directions perpendicular and parallel to the plane spanned by the vectors  $\hat{\mathbf{p}}$  and  $\hat{\mathbf{k}}$  (the radiation plane) are, respectively,

$$\hat{\mathbf{e}}_{\perp} = \frac{\hat{\mathbf{p}} \times \hat{\mathbf{k}}}{|\hat{\mathbf{p}} \times \hat{\mathbf{k}}|}, \quad (13)$$

$$\hat{\mathbf{e}}_{\parallel} = \frac{\hat{\mathbf{k}} \times (\hat{\mathbf{p}} \times \hat{\mathbf{k}})}{|\hat{\mathbf{p}} \times \hat{\mathbf{k}}|}. \quad (14)$$

Then  $\hat{\mathbf{e}}_{\perp}$  is rotated by angle  $\chi$  (see Fig. 2) with respect to the  $y$  direction, which is the perpendicular polarization direction in the reference plane  $xz$  that contains the line of sight  $\hat{\mathbf{k}}$  and the symmetry axis  $\mathbf{B}$ . The angle  $\chi$  is expressed as

$$\cos \chi = \hat{\mathbf{e}}_{\perp y} = (\sin \theta \cos \theta_0 - \cos \theta \sin \theta_0 \cos \phi_0) / \sin \theta', \quad (15)$$

where  $\theta'$  is the angle between  $\hat{\mathbf{p}}$  and  $\hat{\mathbf{k}}$ :

$$\cos \theta' = \cos \theta \cos \theta_0 + \sin \theta \sin \theta_0 \cos \phi_0. \quad (16)$$

Linear polarization (for unpolarized electrons, bremsstrahlung photons are never circularly polarized) is described by the two independent Stokes parameters  $P_1$  and  $P_2$ :  $P_1$  corresponds to the degree of polarization with respect to a given reference plane ( $xz$  in our case);  $P_2$  to the degree of polarization with respect to a plane rotated around the line of sight by  $\pi/4$  from the reference plane. For a given momentum of the initial electron,  $P_1$  and  $P_2$ , normalized by the total intensity, are transformed by rotation of the radiation plane relative to the reference plane as

$$P_{1,\hat{\mathbf{p}}} = \cos 2\chi \frac{d^2 \sigma_1}{d^2 \sigma_0},$$

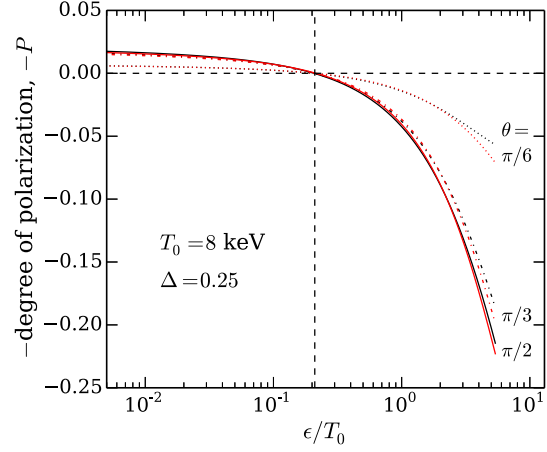


**Figure 3.** The degree of bremsstrahlung polarization from a cloud of electrons with a bi-Maxwellian distribution at temperature  $T_0 = 8$  keV and anisotropy level  $\Delta = 0.25$  [equation (23)] as a function of the emitted photon energy  $\epsilon$  and the angle between the axis of anisotropy and the line of sight. Results in the linear approximation [equations (24) and (25)] are shown in red for comparison. The polarization degree is plotted with the minus sign to facilitate comparison with Fig. 1. The opposite sign comes from the fact that the electron pressure anisotropy  $\Delta$  is defined to be positive for  $T_{\perp} > T_{\parallel}$  [equation (23)].

$$P_{2,\hat{\mathbf{p}}} = \sin 2\chi \frac{d^2 \sigma_1}{d^2 \sigma_0}. \quad (17)$$

Thus, knowing the expression for the angle  $\chi$  [equation (15)] between the radiation and reference planes, we can calculate the degree of polarization of bremsstrahlung emission from a cloud of electrons  $P_{1,2} = \mathcal{I}_{1,2}/\mathcal{I}_0$ , where  $\mathcal{I}_{1,2}$  is the intensity of the polarized emission and  $\mathcal{I}_0$  the total intensity, both integrated over the electron distribution  $F(\varepsilon, \theta_0)$ :

$$\mathcal{I}_0(\varepsilon, \theta) = n_i \int_{\varepsilon}^{\infty} d\varepsilon \int_{-1}^1 d(\cos \theta_0) \int_0^{2\pi} d\phi_0 \times [v(\varepsilon)F(\varepsilon, \theta_0) d^2 \sigma_0(\varepsilon, \varepsilon, \theta')], \quad (18)$$

$$\mathcal{I}_1(\varepsilon, \theta) = n_i \int_{\varepsilon}^{\infty} d\varepsilon \int_{-1}^{+1} d(\cos \theta_0) \int_0^{2\pi} d\phi_0 \times [v(\varepsilon)F(\varepsilon, \theta_0) \cos 2\chi d^2 \sigma_1(\varepsilon, \varepsilon, \theta')], \quad (19)$$

$$\mathcal{I}_2(\varepsilon, \theta) = n_i \int_{\varepsilon}^{\infty} d\varepsilon \int_{-1}^{+1} d(\cos \theta_0) \int_0^{2\pi} d\phi_0 \times [v(\varepsilon)F(\varepsilon, \theta_0) \sin 2\chi d^2 \sigma_1(\varepsilon, \varepsilon, \theta')]. \quad (20)$$

Due to the axisymmetry of the electron distribution function,  $\mathcal{I}_2$  integrates to zero (see, e.g., the appendix of Haug 1972 for a mathematical proof of this), and the total degree of linear polarization is  $P = \mathcal{I}_1/\mathcal{I}_0$ .

The distribution function  $F(\varepsilon, \theta_0)$  is related to the velocity distribution function  $f(v, \theta_0)$  as

$$F(\varepsilon, \theta_0) = v^2 f(v, \theta_0) \frac{dv}{d\varepsilon}. \quad (21)$$

For the velocity distribution function, we employ a bi-Maxwellian:

$$f(v, \theta_0) = n_e \left( \frac{m_e}{2\pi T_{\perp}} \right) \left( \frac{m_e}{2\pi T_{\parallel}} \right)^{1/2}$$

$$\times \exp \left[ -\frac{m_e v^2}{2T_0} \left( \frac{T_0}{T_\perp} \sin^2 \theta_0 + \frac{T_0}{T_\parallel} \cos^2 \theta_0 \right) \right]. \quad (22)$$

where  $T_0 = (1/3)T_\parallel + (2/3)T_\perp$  is the total temperature. If the anisotropy

$$\Delta \equiv \frac{T_\perp - T_\parallel}{T_0} \quad (23)$$

is small and  $\Delta m_e v^2 / (2T_0) \ll 1$ , one can expand the distribution function to the first order in  $\Delta$ :

$$f(v, \theta_0) = f_0(v) + \delta f_\Delta(v, \theta_0), \quad (24)$$

where  $f_0(v)$  is an isotropic Maxwell distribution at temperature  $T_0$ :

$$f_0(v) = n_e \left( \frac{m_e}{2\pi T_0} \right)^{3/2} \exp \left( -\frac{m_e v^2}{2T_0} \right) \quad (25)$$

and the anisotropic perturbation is

$$\delta f_\Delta(v, \theta_0) = \Delta \frac{m_e v^2}{2T_0} \left( \frac{1}{3} - \cos^2 \theta_0 \right) f_0(v). \quad (26)$$

Using equations (20), (21), and (26), we obtain the degree of polarization of thermal bremsstrahlung for a small anisotropic perturbation of the electron distribution, when the linear approximation [expansion in  $\Delta$  in equation (24)] is applicable:

$$P(\epsilon, T_0, \theta) = \Delta \sin^2 \theta G(\epsilon, T_0), \quad (27)$$

where  $G(\epsilon, T_0)$  becomes a function of  $\epsilon/T_0$  at temperatures  $T_0 \lesssim 10$  keV. At  $\epsilon \sim$  a few  $T_0$ ,  $G(\epsilon, T_0) \sim 1$ . The degree of polarization from a cloud of anisotropic electrons with  $\Delta = 0.25$  at  $T_0 = 8$  KeV is shown in Fig. 3 in black for a general bi-Maxwellian distribution, and in red in the linear approximation [equation (27)]. We see that the linear approximation holds at least up to  $\Delta \approx 0.25$ .

### 3 APPLICATION TO COLD FRONTS AND SHOCKS IN THE ICM

#### 3.1 Qualitative estimates

Cold fronts are sharp discontinuities of temperature and density seen in X-rays in a number of clusters (Markevitch et al. 2000; Ettori & Fabian 2000; Vikhlinin et al. 2001; Markevitch & Vikhlinin 2007). These are commonly associated with a flow of the hot ambient ICM plasma around a cold subcluster moving in the host cluster nearly at the virial speed. The plasma flow produces draping of the frozen-in magnetic-field lines over the cold cloud (e.g., Lyutikov 2006; Asai et al. 2007; Dursi & Pfrommer 2008). Near the front, the flow is essentially a convergence flow, and the field lines are continuously stretched along the interface. This leads to perpendicular orientation of the field lines and temperature gradient and likely inhibits thermal conduction, preserving the sharp gradient between the cold cloud and hot ICM over dynamically long times (e.g., Vikhlinin & Markevitch 2002).

The field-line stretching should naturally produce pressure anisotropy. In Section 2.1, we made simple estimates of the degree of pressure anisotropy for a sonic flow of plasma. These depend on three parameters: the collisional mean free

path  $\lambda$  and the characteristic scales of the flow  $L_u$  and parallel temperature gradient  $L_T$ . Let us now estimate the typical electron anisotropy induced by the magnetic-field evolution at the interface of a cold front. Because the subcluster is moving at around the virial speed, the flow of the hot ICM in the comoving frame is nearly sonic. From equation (11) with  $u \sim v_{th,i}$ , we get  $\Delta_B \sim (1/40)\lambda/L_u \sim 2 \times 10^{-3}$ , where for cold fronts we took the electron mean free path  $\lambda \sim 20$  kpc ( $T \sim 8$  keV) and the flow scale  $L_u \sim 200$  kpc [of order the size of the subcluster, e.g., A3667 (Markevitch & Vikhlinin 2007)]. The degree of polarization is a few times smaller than the anisotropy level, because the coherently anisotropic plasma occupies only a fraction of volume of the X-ray emitting ICM, and the magnetic-field direction is not necessarily perpendicular to the line of sight. Below, we investigate the amount of electron anisotropy, the corresponding bremsstrahlung polarization, and their spatial patterns in cold fronts first by means of the simplest analytical model of magnetic-field-line draping (Section 3.2), and then by numerical MHD simulations of cold fronts with anisotropic thermal conduction (Section 3.3). We also estimate the total anisotropy for the simulated cold fronts in Appendix A.

#### 3.2 Analytical model of magnetic-field-line draping

The problem of the stationary MHD flow of a plasma with a frozen-in magnetic field around a spherical body was first solved analytically by Bernikov & Semenov (1979). They disregarded the magnetic-field back-reaction and assumed a velocity field described by the potential flow of an incompressible irrotational fluid around a sphere. Here we briefly summarize their derivation and use the resulting magnetic field near the body to calculate electron pressure anisotropy and thermal bremsstrahlung polarization.

In spherical coordinates with the origin at the center of the sphere of radius  $R$  and the  $z$  axis antiparallel to the fluid velocity  $v_0$  at infinity, the potential flow around the sphere is

$$\mathbf{v} = e_r \left( \frac{R^3}{r^3} - 1 \right) v_0 \cos \theta + e_\theta \left( \frac{R^3}{2r^3} + 1 \right) v_0 \sin \theta. \quad (28)$$

The magnetic field is obtained by solving the stationary ideal MHD equations

$$\nabla \times (\mathbf{v} \times \mathbf{B}) = 0, \quad \nabla \cdot \mathbf{B} = 0, \quad (29)$$

with a homogeneous magnetic field  $B_0$  along the  $y$  axis at infinity in the left-half space ( $z < 0$ ) as the boundary condition. We are primarily interested in the approximate solution near the sphere ( $r - R \ll R$ ), where stretching of the field lines is greatest. It reads

$$\begin{aligned} B_r &= \frac{2}{3} B_0 \sqrt{3(r/R - 1)} \frac{\sin \theta}{1 + \cos \theta} \sin \phi, \\ B_\theta &= B_0 \frac{\sin \phi}{\sqrt{3(r/R - 1)}}, \\ B_\phi &= B_0 \frac{\cos \phi}{\sqrt{3(r/R - 1)}}. \end{aligned} \quad (30)$$

The velocity and magnetic fields are shown in the left panel of Fig. 4.

We can now apply equation (10), where only the first

term on the right-hand side has to be kept, to calculate the electron anisotropy  $\Delta$ . The term  $\Delta_n$  is zero because the flow is incompressible. The heat-flux contribution to electron anisotropy  $\Delta_T$  is also zero because in our configuration, the cold cloud is completely isolated from the hot ambient plasma by the draped field lines. We choose to ignore temperature variations of the incompressible gas outside the sphere and assume homogeneous temperature, because these variations would otherwise be clearly overstated due to the artificial assumption of constant density. Then

$$\Delta = \Delta_B = \frac{\gamma}{\nu_e}. \quad (31)$$

From the induction equation, we obtain the rate of stretching of the field lines  $\gamma$ :

$$\gamma \equiv \frac{1}{B} \frac{dB}{dt} = \mathbf{b}\mathbf{b} : \nabla \mathbf{v}, \quad (32)$$

where  $\mathbf{b} = \mathbf{B}/B$  is the unit vector in the direction of the magnetic field. The electron collision frequency (Spitzer 1962) in a hydrogen plasma is

$$\nu_e \approx 3 \times 10^{-6} \text{ yr}^{-1} \left( \frac{T_e}{8 \text{ keV}} \right)^{3/2} \left( \frac{n_e}{10^{-3} \text{ cm}^{-3}} \right)^{-1}. \quad (33)$$

We take the radius of the sphere  $R = 200 \text{ kpc}$ , temperature  $T_0 = 8 \text{ keV}$  and particle density  $n_0 = 10^{-3} \text{ cm}^{-3}$  as fiducial parameters. Let us set the flow velocity at infinity  $v_0$  to the speed of sound  $c_{s0} = (\gamma_{\text{gas}} p_0 / \rho_0)^{1/2} \approx 1400 \text{ km/s}$ . Combining equations (28)–(33), we can calculate the electron anisotropy  $\Delta$ . It is shown in the middle panel of Fig. 4 in the central  $yz$  cross section. Its value agrees well with the previous qualitative estimate in Section 3.1.

The final step is to obtain the polarization of thermal bremsstrahlung from the linear approximation (27), which is, indeed, satisfied for our typical values of electron anisotropy  $\Delta \sim (1-5) \times 10^{-3}$ . We only consider the case of sufficiently energetic photons ( $\epsilon \sim 2-3 T_e$ ) in the hard X-ray range to ignore the photon-energy/electron-temperature dependence and assume  $G \sim 1$  in equation (27). To obtain the polarization map, we need to integrate equation (27) weighted with the thermal bremsstrahlung emissivity  $\kappa_{\text{br}}$ ,

$$\kappa_{\text{br}} \propto n_e^2 T_e^{-1/2} \exp(-\epsilon/T_e), \quad (34)$$

along the line of sight <sup>2</sup>, taking into account the rotation of the polarization vectors due to the changing orientation of the magnetic field. Here and in what follows, we simply assume that the X-ray emitting volume is restricted to a cubic region of size  $5R = 1 \text{ Mpc}$ , ignoring the effects of the geometry of the host cluster and the location of the cold front inside the host cluster. This should not change our results qualitatively, only introducing a large-scale factor of order unity to the anisotropy and polarization degree. Because the plasma flow is incompressible in our toy model, and its temperature is taken to be homogeneous, the emissivity is a constant outside the sphere. We choose the  $x$  axis as the direction of the line of sight, because in this direction, the polarization is greatest, and  $xy$  as the reference plane. We

<sup>2</sup> The exact temperature dependence may be slightly different if the correct form of the gaunt factor is adopted, but it practically does not affect our results because of small temperature variations outside of the cold cloud.

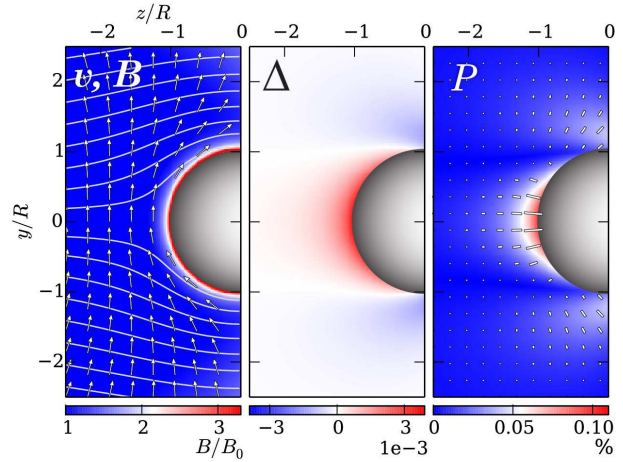


**Figure 4.** Generation of pressure anisotropy and thermal bremsstrahlung polarization during kinematic draping of magnetic-field lines around a spherical body. The velocity field is the potential flow of an incompressible fluid around a sphere [equation (28)]. The magnetic field is an approximate solution of the ideal kinematic MHD equations near the sphere [equations (30)]. The left and middle panels are the central  $yz$  cross sections. *Left:* the magnetic-field strength  $B$  (color) in the units of  $B$  at infinity,  $B_0$ ; superimposed are the velocity field streamlines (contours) and the unit vectors in the direction of the magnetic field (arrows). *Middle:* the electron pressure anisotropy generated by stretching of the field lines by the flow. *Right:* the degree (color) and direction (line segments) of the polarization of thermal bremsstrahlung as seen along the line of sight coincident with the  $x$  axis).

have to integrate both of the independent linear polarization types,  $P_1$  and  $P_2$ , where  $P_1$  is the polarization measured in the vector basis  $(\hat{e}_y, \hat{e}_z)$ , and  $P_2$  measured in the basis rotated by  $\pi/4$  from  $(\hat{e}_y, \hat{e}_z)$ . The local polarizations  $P_{1,\text{loc}}$  and  $P_{2,\text{loc}}$  relative to the reference plane  $xy$  are expressed in terms of polarization  $P_{B,\text{loc}}$  [equation (27)] relative to the plane spanned by the local magnetic-field direction and the line of sight ( $x$  axis):

$$P_{1,\text{loc}} = P_{B,\text{loc}} \cos(2\zeta), \quad (35)$$

$$P_{2,\text{loc}} = P_{B,\text{loc}} \sin(2\zeta), \quad (36)$$

where  $\zeta$  the angle between the projection of the magnetic field onto the  $yz$  plane and the  $y$  axis. Using equation (27) for  $P_{B,\text{loc}}$  and integrating the local polarization along the line of sight, we get

$$P_1 = \frac{\int \Delta \sin^2 \theta \cos(2\zeta) \kappa_{\text{br}} dx}{\int \kappa_{\text{br}} dx}, \quad (37)$$

$$P_2 = \frac{\int \Delta \sin^2 \theta \sin(2\zeta) \kappa_{\text{br}} dx}{\int \kappa_{\text{br}} dx}, \quad (38)$$

where  $\theta$  is the angle between the local magnetic field and the line of sight [as in equation (27)]. The angles  $\theta$  and  $\zeta$  can be expressed in terms of the components of the unit vector in the direction of the field  $\mathbf{b}$ :

$$\cos 2\zeta = (b_y^2 - b_z^2)/(b_y^2 + b_z^2), \quad (39)$$

$$\sin^2 \theta = 1 - b_x^2. \quad (40)$$

The total linear polarization  $P$  is

$$P = (P_1^2 + P_2^2)^{1/2}. \quad (41)$$

The polarization position angle relative to  $\hat{\mathbf{e}}_y$  is set by angle  $\psi$ ,

$$\psi = \frac{1}{2} \text{atan} \frac{P_2}{P_1}. \quad (42)$$

The resulting thermal bremsstrahlung polarization pattern is shown in the right panel of Fig. 4, where color indicates the degree of polarization, and line segments the position angles [calculated by equation (42)] in the  $yz$  plane. The characteristic degree of polarization is  $\sim 0.1\%$ . If we integrate the polarization along a line of sight at angle  $\theta' \neq 0$  to the  $x$  axis instead, the effect becomes a factor of  $\cos^2 \theta'$  smaller from the form of equations (37) and (38).

### 3.3 MHD simulations of cold fronts

#### 3.3.1 Description of the code and setup

To simulate cold fronts for the purpose of this work, we use an MHD code based on the van Leer integrator combined with the constrained transport (CT) approach (see Stone & Gardiner 2009 for a description of the numerical method). Anisotropic thermal conduction was implemented via a semi-implicit directionally-split scheme with a monotized central (MC) limiter applied to the conductive fluxes to avoid negative temperatures (Sharma & Hammett 2011). The set of equations solved is

$$\frac{\partial \rho}{\partial t} + \nabla \cdot (\rho \mathbf{v}), \quad (43)$$

$$\frac{\partial \rho \mathbf{v}}{\partial t} + \nabla \cdot \left( \rho \mathbf{v} \mathbf{v} - \frac{\mathbf{B} \mathbf{B}}{4\pi} \right) + \nabla p = \rho \mathbf{g}, \quad (44)$$

$$\frac{\partial E}{\partial t} + \nabla \cdot \left[ \mathbf{v}(E + p) - \frac{\mathbf{B}(\mathbf{v} \cdot \mathbf{B})}{4\pi} \right] = \rho \mathbf{g} \cdot \mathbf{v} - \nabla \cdot \mathbf{Q}, \quad (45)$$

$$\frac{\partial \mathbf{B}}{\partial t} = \nabla \cdot (\mathbf{v} \mathbf{B} - \mathbf{B} \mathbf{v}), \quad (46)$$

where

$$p = p_{\text{th}} + \frac{B^2}{8\pi}, \quad (47)$$

$$E = \frac{\rho v^2}{2} + \varepsilon + \frac{B^2}{8\pi}, \quad (48)$$

$$\mathbf{Q} = -\kappa_{\parallel} \mathbf{b} \mathbf{b} : \nabla T, \quad (49)$$

where  $p_{\text{th}}$  is the gas pressure,  $\varepsilon$  the internal energy of the plasma per unit volume,  $\mathbf{g}$  the gravitational acceleration, and  $\mathbf{Q}$  the heat flux along the field lines with parallel thermal conductivity  $\kappa_{\parallel}$ . The plasma is described by an ideal equation of state with  $\gamma_{\text{gas}} = 5/3$  and mean molecular weight  $\mu = 0.6$ . We take the fiducial value of  $\kappa_{\parallel} = \kappa_{\text{Sp}}$ , where  $\kappa_{\text{Sp}}$  is the Spitzer thermal conductivity for an unmagnetized plasma (Spitzer 1962). We ignore any potential mechanisms whereby parallel thermal conduction might be suppressed (e.g., magnetic mirrors, Chandran & Cowley 1998; Komarov et al. 2016, or electron kinetic instabilities, Riquelme et al. 2016), as we are looking for an upper estimate of the polarization effect.

We initialize a 3D region of hot dilute plasma ( $T_{\text{out}} = 8$  keV,  $n_{\text{out}} = 10^{-3} \text{ cm}^{-3}$ ) of spatial extent  $L = 1$  Mpc with a cold spherical subcluster ( $T_{\text{in}} = 4$  keV) of radius  $R = 200$  kpc embedded at the center. The distribution of density inside the cold cloud is described by a beta model,

$$n_{\text{in}} = n_c [1 + (r/r_c)^2]^{-3\beta'/2}, \quad (50)$$

with  $\beta' = 2/3$ , core radius  $r_c = R/\sqrt{3} \approx 115$  kpc, and central density  $n_c = 8n_{\text{out}}$ . The gravitational acceleration  $\mathbf{g}$  models the effect of a static dark matter halo at the center of the computational domain, and is set to balance the initial pressure gradient inside the subcluster. The edge of the subcluster at  $r = R$  is a contact discontinuity: the temperature experiences a factor-of-two jump in the direction of the hot ambient plasma, while the density decreases by a factor of two to keep the pressure continuous. The problem is solved in the frame comoving with the subcluster. Initially, the cold cloud is at rest, while the velocity of the surrounding gas  $v_0$  is set to the sound speed in the hot ambient plasma,  $c_{s0} = (\gamma_{\text{gas}} p_{\text{out}} / \rho_{\text{out}})^{1/2} = (\gamma_{\text{gas}} k T_{\text{out}} / \mu m_p)^{1/2} \approx 1400$  km/s. This setup is similar to the one used by Asai et al. (2007).

To make estimates of the bremsstrahlung polarization generated by electron pressure anisotropy due to stretching of the magnetic-field lines and to heat fluxes, we analyze the results of two runs with different structure of the magnetic field. In both runs, the initial plasma  $\beta = 200$ . The first run is initialized with a homogeneous magnetic field along the  $y$  axis, perpendicular to the cold cloud velocity. The initial magnetic field in the second run is random with a Gaussian distribution and correlation length  $l_B = L/10 \approx 100$  kpc. We note that the statistics of magnetic fields in galaxy clusters are unlikely to be Gaussian, and the reported values of the correlation length inferred from the Faraday rotation observations are about an order of magnitude smaller (e.g., Vogt & Enßlin 2005). Therefore, this run is merely illustrative and demonstrates only qualitative differences between cases with uniform and tangled magnetic field.

#### 3.3.2 Results for the case of a homogeneous magnetic field

The central  $yz$  cross sections of the plasma temperature  $T$ , velocity field  $\mathbf{v}$  and magnetic field  $\mathbf{B}$  are shown in the top left and top middle panels of Fig. 5 at time  $t \approx 0.3$  Gyr. The anisotropy pattern at the cold front interface is similar to the one in the analytical model of the field-line draping (top right panel of Fig. 5), with the typical magnitude of the anisotropy  $\Delta \sim 10^{-3}$ . Using the continuity and induction equations, we can express the degree of anisotropy produced by the field-line stretching and compression of the gas as

$$\Delta_B + \Delta_n = \frac{1}{v_e} \left( \mathbf{b} \mathbf{b} : \nabla \mathbf{v} - \frac{1}{3} \nabla \cdot \mathbf{v} \right). \quad (51)$$

Compression contributes via the divergence of the velocity field  $\nabla \cdot \mathbf{v}$ . Because  $\nabla \cdot \mathbf{v}$  is positive ahead of the subcluster, the electron anisotropy at the interface is reduced compared to the incompressible model. The sharp boundary of the anisotropy pattern ahead of the front is due to a discontinuity in the static gravitational acceleration, which is set to zero outside the sphere of radius  $R$ . This does not affect our estimate of the degree of polarization and of the size of the polarized region. Because the magnetic field points in the  $y$  direction initially, the heat flux across the interface is fully suppressed, while in the regions where the orientation of the field lines is not perfectly perpendicular to the temperature gradients, the heat flux contribution is noticeable (see the bottom left panel of Fig. 5).

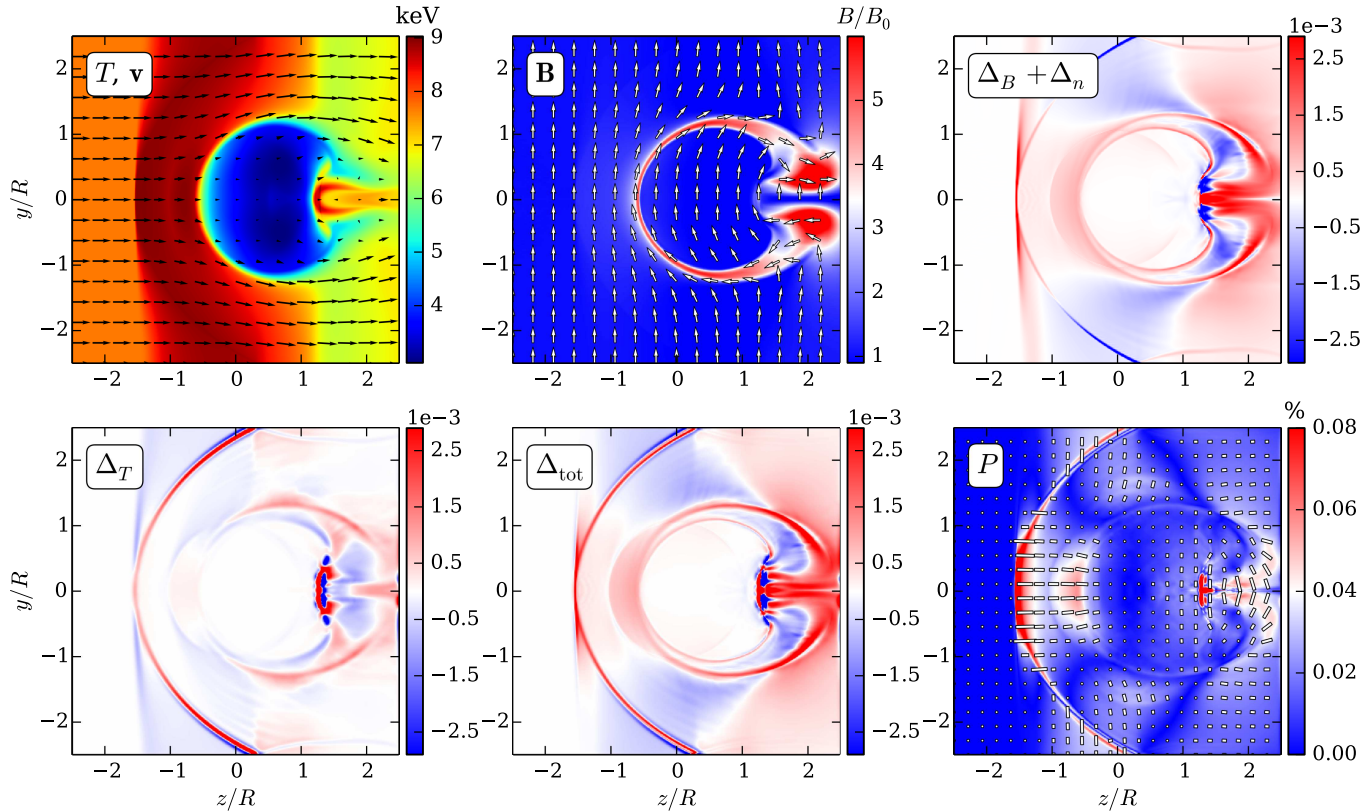


**Figure 5.** A simulation of a cold front with a homogeneous initial magnetic field along the  $y$  direction. All the panels except for the bottom right are the central  $yz$  cross sections at time  $t \approx 0.3$  Gyr. The top left panel shows the temperature map (color) and the velocity field (arrows). The magnetic field  $\mathbf{B}$  is shown in the top middle panel (color: field strength; arrows: unit vectors in the magnetic-field direction). The different components of the electron anisotropy and the total electron anisotropy are demonstrated in the top right, bottom left, and bottom middle panels. The bottom right panel shows the resulting polarization map in the  $x$  direction.

The new features of the simulated cold front, compared to the simplistic analytical model studied in Section 3.2, are the presence of a weak bow shock in front of the subcluster and the formation of turbulent vortices that efficiently amplify the magnetic field behind the subcluster. Let us analyze them in more detail.

At the moment of taking the snapshot shown in Fig. 5 ( $t \approx 0.3$  Gyr), the bow shock is slowly receding from the cold front at speed  $u_{\text{sh}} \approx 250$  km/s. Let us first discuss the contribution to the anisotropy at the shock brought in by the compression of the gas. The source of the anisotropy is the jump of the normal velocity and tangential component of the magnetic field at the shock close to the  $z$  axis. The passage of the shock amplifies the  $y$  component of the magnetic field in the downstream flow. From equation (51) with  $\mathbf{bb} : \nabla \mathbf{v} = 0$  (close to the  $z$  axis, the velocity only changes in the direction perpendicular to the field lines), we can estimate the anisotropy  $\Delta_B + \Delta_n$  at the shock:

$$\Delta_{B,\text{sh}} + \Delta_{n,\text{sh}} \sim -10^{-2} \frac{v_{z,\text{d}} - v_{z,\text{u}}}{c_{s0}} \frac{\lambda}{\delta}, \quad (52)$$

where  $v_{z,\text{u}}$  and  $v_{z,\text{d}}$  are the up- and downstream normal velocities,  $\delta$  the width of the shock, and  $\lambda$  the electron mean free path. The normal velocity discontinuity contributes to the electron anisotropy via the non-zero velocity divergence.

The upstream velocity is the speed of sound,  $v_{z,\text{u}} = v_0 = c_{s0}$ , while the normal velocity jump in the frame of the shock from the Rankine-Hugoniot conditions (consider the magnetic field dynamically unimportant) is

$$\frac{v_{z,\text{d}} + u_{\text{sh}}}{v_{z,\text{u}} + u_{\text{sh}}} = \frac{(\gamma_{\text{gas}} + 1)M_1^2}{(\gamma_{\text{gas}} - 1)M_1^2 + 2} \approx 0.8, \quad (53)$$

where  $M_1 = (v_{z,\text{u}} + u_{\text{sh}})/c_{s0} \approx 1.18$  is the Mach number of the upstream gas in the frame of the shock. Then we can infer the velocity jump in laboratory frame  $v_{z,\text{d}}/v_{z,\text{u}} \approx 0.8$ . Taking the shock width  $\delta \sim \lambda$ , from equation (52) we estimate the typical value of anisotropy at the shock  $\Delta_{B+n,\text{sh}} \approx 2 \times 10^{-3}$ . Results of the numerical simulations agree well with this estimate (see the top right panel of Fig. 5). At angles larger than  $\pi/4$  from the  $z$ -axis, the term  $\mathbf{bb} : \nabla \mathbf{v} \approx b_y^2 \partial_y v_y < 0$  starts to dominate at the shock, because there is a jump in the  $y$ -velocity parallel to the field lines, and the magnetic field is compressed along the  $y$  direction producing negative electron anisotropy.

Close to the  $z$  axis, the magnetic field is perpendicular to the temperature gradient, and there is no heat flux across the shock. However, away from the  $z$  axis, the magnetic field only partly impedes thermal conduction. Although the strong parallel conductivity smears the temperature gradient, a small jump of the temperature and its gradient



along the shock is still left behind. The jump  $\delta T/T$  is of order 0.5 %, and the level of positive anisotropy it generates is of the same order, because, from equation (12),  $\Delta_T \sim (\lambda/L_T)^2 \delta T/T$  (we took  $L_u = L_T$  because the heat flux changes at the scale of the shock width, as well as the temperature). The scale of the gradient  $L_T$  is of the order of the shock width, which can be approximated by the mean free path  $\lambda$ . Then the anisotropy is simply  $\Delta_T \sim \delta T/T \sim 0.5$  %. This is seen in the bottom left panel of Fig. 5.

Another notable feature of the simulated cold front is the amplification of the magnetic field behind the subcluster (top middle panel of Fig. 5), previously reported by Asai et al. (2007). The amplification is caused by stretching of the field lines along the  $z$  direction by the vortices generated by the flow of the ambient gas around the subcluster. The magnetic field is amplified more efficiently than at the cold front interface, because the vortices are smaller than the subcluster, and thus produce a velocity strain rate larger than that ahead of the subcluster by a factor of the ratio of the subcluster size to the size of the vortices. Therefore, they are expected to generate more electron anisotropy, which is clearly seen in the top right panel of Fig. 5.

The total electron anisotropy is shown in the bottom middle panel of Fig. 5. The corresponding polarization of thermal bremsstrahlung is calculated by equations (34)–(42), now taking account of the spatial variation of the bremsstrahlung emissivity [equation (34)], and demonstrated in the bottom right panel of Fig. 5. The polarization is generally dominated by stretching of the field lines and the compressibility effects. There are three regions where the degree of polarization is at  $\sim 0.1\%$  level: 1) at the cold-front interface due to stretching of the field lines in the  $y$  direction; 2) at the bow shock close to the  $z$  axis due to the compressibility term in equation (51); 3) behind the subcluster due to amplification of the magnetic field along the  $z$  direction by the turbulent vortices.

### 3.3.3 Results for the case of a random magnetic field

It is currently believed (based on numerical and indirect observational evidence) that the ICM is turbulent (see, e.g., Inogamov & Sunyaev 2003; Schuecker et al. 2004; Schekochihin & Cowley 2006; Subramanian et al. 2006; Zhuravleva et al. 2014), and, therefore, the magnetic fields in the ICM are tangled by random motions of the plasma. Here we model the effect of random topology of the field lines by generating a random Gaussian magnetic field with correlation length  $l_B = 100$  kpc. The mean plasma  $\beta = 2p_{\text{out}}/\langle B^2 \rangle = 200$ , where  $\langle B^2 \rangle = B_0^2$ . Analogously to the case of a homogeneous magnetic field, the results of our simulations are shown in Fig. 6. The random field topology diminishes the electron anisotropy produced by stretching of the field lines at the cold-front interface (top right panel of Fig. 6) and almost completely wipes out its contribution to the total polarization (see the bottom right panel). We should remark that due to numerical diffusivity, during compression and stretching of the field-line loops by the convergence flow at the front, the opposite orientations of the field may reconnect, thus modifying the field-line topology in the region where one expects to see electron anisotropy. Therefore, our numerical estimate in this region might be understated.

Because now the field-line orientation at the bow shock is random, in addition to the compression term [equation (52)], the heat fluxes also positively contribute to the total anisotropy everywhere across the shock (see the bottom left panel of Fig. 6). The level of electron anisotropy generated by the turbulent vortices behind the shock is practically unchanged compared to the simulation with a homogeneous magnetic field. In a random magnetic field, this mechanism appears to be the most efficient.

The resulting polarization map (bottom right panel) indicates that 1) polarization at the cold-front interface is practically indiscernible; 2) the degree of polarization at the shock is  $\sim 0.05\%$ ; 3) the largest polarization,  $\sim 0.1\%$ , is achieved behind the cold cloud via the magnetic-field amplification by the turbulent backflow.

## 4 DISCUSSION

At present, the only astrophysical object from which a polarized signal has been reliably detected in X-rays below 10 keV is the Crab Nebula (Weisskopf et al. 1978), dating back to the 70s. The progress with the development of the new generation of X-ray polarimeters (e.g., Soffitta et al. 2013; Weisskopf et al. 2013; Jahoda et al. 2014) has led to a dramatic increase of the expected sensitivity that could open a new observational window into a variety of astrophysical objects. Magnetars, radio and accreting X-ray pulsars, reflected radiation in X-ray binaries or AGNs are all among the promising targets for missions like XIPE, IXPE and PRAXyS.

In the majority of those objects, polarization is either associated with non-thermal emission (e.g., synchrotron radiation of relativistic electrons) or with scattering in aspherical geometries. Here we discuss the polarization of *thermal* emission from the hot gas in galaxy clusters. This is an interesting question for at least two reasons: (i) clusters of galaxies are considered as possible unpolarized targets for calibration purpose and (ii) weak polarization of thermal bremsstrahlung potentially could serve as a proxy for the plasma properties on extremely small scales, not directly resolvable with the current or future X-ray missions.

As we showed in the previous sections, the polarization of thermal bremsstrahlung naturally arises from the anisotropy of the electron distribution function driven by stretching of the magnetic-field lines and/or temperature gradients along the field. Pitch-angle scattering of the electrons controls the level of anisotropy, and even if it is set purely by Coulomb collisions, the anisotropy is always small. Further reduction of the observed polarization signal is expected if many uncorrelated regions with varying orientation of anisotropy are present along the line of sight, leading to effective averaging of the signal. From this point of view, the most promising are the configurations with a large-scale flow that provides a coherence of structures and drives the anisotropy. Our qualitative estimates show that the expected degree of polarization is close to 0.1% for rather idealized configurations that exhibit shocks and cold fronts.

It is worth noting that aside from polarizing thermal bremsstrahlung, electron pressure anisotropy is also capable of producing a small degree of polarization of the Sunyaev-Zeldovich (SZ) signal (Sunyaev & Zeldovich

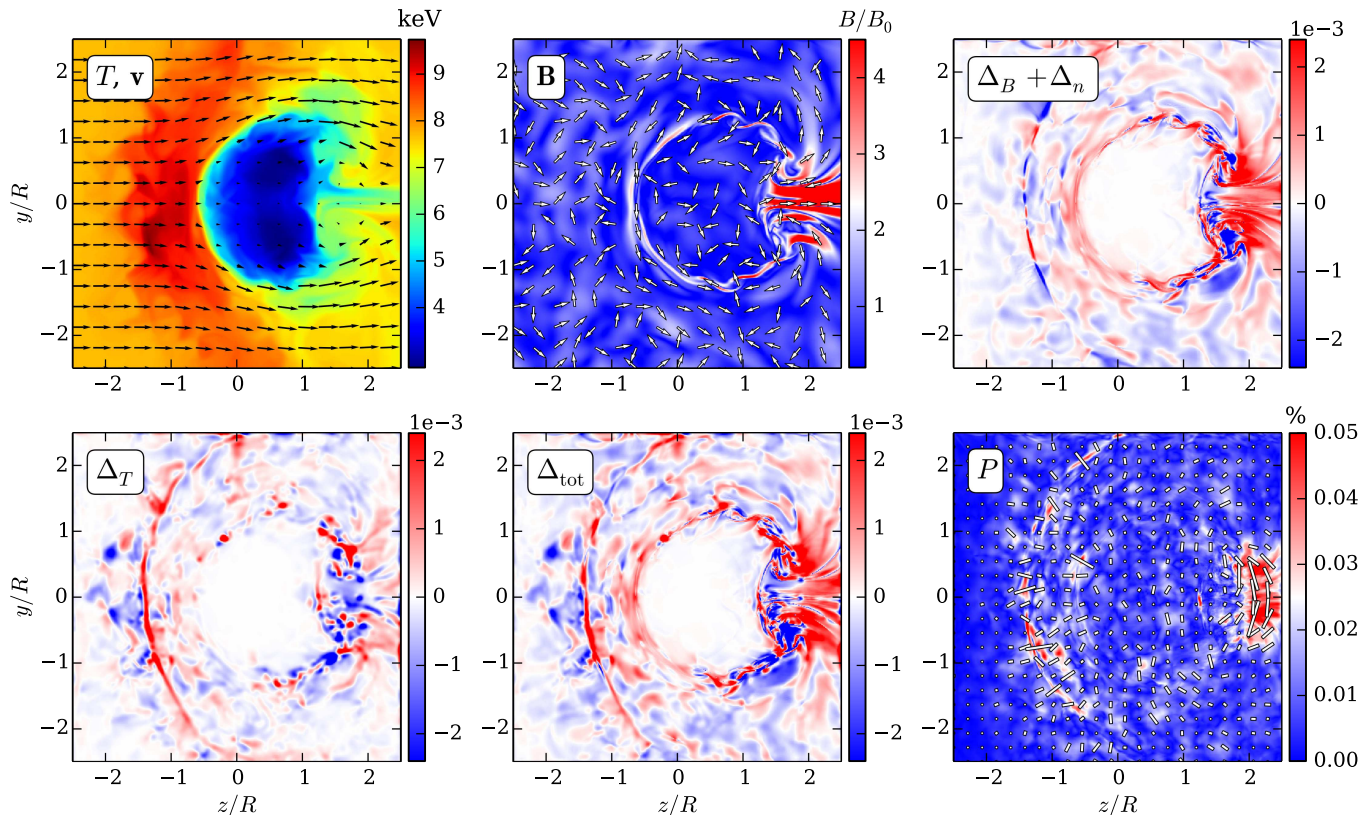


**Figure 6.** A simulation of a cold front with a random Gaussian initial magnetic field with correlation length  $l_B \approx 100$  kpc. The panels show the same quantities as in Fig. 5.

1980) and the emission in collisionally-excited X-ray lines (e.g., He-like triplets of silicon, sulphur and iron, see Pal'chikov & Shevelko 1995, p. 140, and references therein). However, these two effects are both subjected to somewhat higher possible contamination coming from the Thomson scattering of cluster central AGN radio emission and the contribution of the kinetic SZ effect in the first case (Sunyaev & Zeldovich 1980; Sazonov & Sunyaev 1999; Diego et al. 2003), and resonant-scattering-induced polarization in the latter case (Sazonov et al. 2002; Zhuravleva et al. 2010).

The small degree of polarization makes galaxy clusters a suitable (unpolarized) calibration target for the forthcoming generation of X-ray polarimeters. We note in passing that two other mechanisms could also contribute to the polarization of thermal emission of the hot gas in clusters. One is Thomson scattering of centrally concentrated X-ray emission by the electrons; another is resonant scattering of emission-line photons (Sazonov et al. 2002; Zhuravleva et al. 2010). Both effects have a clear signature of the polarization plane being perpendicular to the direction towards the cluster center and are expected to disappear if the integrated signal (over a circular region around the cluster center) of a relaxed cluster is used. Even if an offset region is considered, one can crudely estimate the expected level of polarization. Given that the Thomson optical depth in clusters is at the level of  $10^{-3}$ , the scattered thermal emission should not be polarized by more than a fraction of

this value. For resonant lines, the optical depth is larger, but the effect is confined to line photons and does not affect the continuum. On the whole, clusters are suitable calibration objects for IXPE, XIPE, or PRAXyS.

Nevertheless, if future polarimeters with capabilities well beyond currently developed instruments could detect polarization from carefully selected clusters with large-scale substructure, it would imply that one has a way to constrain the effective collisionality of electrons. Of course, clusters of galaxies are not the only objects where polarization of thermal emission could be present. As an example one could consider hot radiatively inefficient flows around black holes or neutron stars that might have conditions suitable for generation of sufficient electron anisotropy. We defer this question to further studies.

## 5 CONCLUSIONS

We have studied the effect of polarization of thermal bremsstrahlung emission in a weakly collisional astrophysical plasma due to (small) electron pressure anisotropy. Stretching of magnetic-field lines by a flow of plasma, compression/rarefaction, or heat fluxes all lead to generation of pressure anisotropy in a plasma where the Larmor radii of the charged particles are much smaller than their mean free paths. In the case of ordered plasma motions with a certain preferred direction, electron anisotropies may produce po-

larization of thermal bremsstrahlung emission. The degree of polarization is a few times lower than the anisotropy level (depending on the size of the region of coherently anisotropic electrons and on the bremsstrahlung photon energy).

We have estimated the upper bounds on the degree of polarization in cold fronts in the ICM as they represent a perfect example of converging flows and large temperature gradients. Cold fronts may also be associated with additional features (although not always observed), such as bow shocks or turbulent vortices generated behind subclusters. We have found that a small polarization, at  $\sim 0.1\%$  level, can be generated by either the converging flow, weak bow shock, or vortices behind the cold front. Although at the moment, such a small degree of bremsstrahlung polarization at energies of a few  $kT$  cannot be observed, future observations of this effect might provide a valuable insight into the generation of pressure anisotropies in astrophysical plasmas. The absence of polarization at the estimated level could also set lower limits on electron collisionality in the ICM, which may be enhanced by scattering off microscale magnetic fluctuations (Riquelme et al. 2016) or magnetic trapping by the mirror instability at the scale of the ion Larmor radius (Komarov et al. 2016).

## ACKNOWLEDGEMENTS

The authors thank M. W. Kunz and A. Spitkovsky for useful discussions. EC acknowledges partial support by grant No. 14-22-00271 from the Russian Scientific Foundation. AAS's work was supported in part by grants from the UK STFC and EPSRC.

## REFERENCES

- Asai N., Fukuda N., Matsumoto R., 2007, *ApJ*, 663, 816
- Axford W. I., Leer E., Skadron G., 1977 Vol. 11, The acceleration of cosmic rays by shock waves. Proceedings of the 15th International Cosmic Ray Conference, Plovdiv, Bulgaria, pp 132–137
- Bai T., Ramaty R., 1978, *ApJ*, 219, 705
- Bale S. D., Kasper J. C., Howes G. G., Quataert E., Salem C., Sundkvist D., 2009, *Phys. Rev. Lett.*, 103, 211101
- Bell A. R., 1978, *MNRAS*, 182, 147
- Bernikov L. V., Semenov V. S., 1979, *Geomagnetism and Aeronomy*, 19, 671
- Blandford R. D., Ostriker J. P., 1978, *ApJ*, 221, L29
- Chandran B. D. G., Cowley S. C., 1998, *Phys. Rev. Lett.*, 80, 3077
- Chandrasekhar S., Kaufman A. N., Watson K. M., 1958, *Proc. R. Soc. London A*, 245, 435
- Chew G. F., Goldberger M. L., Low F. E., 1956, *Proc. R. Soc. London A*, 236, 112
- Diego J. M., Mazzotta P., Silk J., 2003, *ApJ*, 597, L1
- Dursi L. J., Pfrommer C., 2008, *ApJ*, 677, 993
- Ettori S., Fabian A. C., 2000, *MNRAS*, 317, L57
- Gluckstern R. L., Hull M. H., 1953, *Phys. Rev.*, 90, 1030
- Hasegawa A., 1969, *Phys. Fluids*, 12, 2642
- Haug E., 1972, *Sol. Phys.*, 25, 425
- Hellinger P., Trávníček P., Kasper J. C., Lazarus A. J., 2006, *Geophys. Res. Lett.*, 33, 9101
- Inogamov N. A., Sunyaev R. A., 2003, *Astron. Lett.*, 29, 791
- Jahoda K. M., Black J. K., Hill J. E., Kallman T. R., Kaaret P. E., Markwardt C. B., Okajima T., Petre R., Soong Y., Strohmayer T. E., Tamagawa T., Tawara Y., 2014, in *Space Telescopes and Instrumentation 2014: Ultraviolet to Gamma Ray* Vol. 9144 of *Proc. SPIE*, X-ray polarization capabilities of a small explorer mission. p. 91440N
- Kasper J. C., Lazarus A. J., Gary S. P., 2002, *Geophys. Res. Lett.*, 29, 1839
- Komarov S. V., Churazov E. M., Kunz M. W., Schekochihin A. A., 2016, *ArXiv: 1603.00524*
- Komarov S. V., Churazov E. M., Schekochihin A. A., ZuHone J. A., 2014, *MNRAS*, 440, 1153
- Krymskii G. F., 1977, *Akademiia Nauk SSSR Doklady*, 234, 1306
- Kulsrud R., 1964, in Rosenbluth M. N., ed., *Advanced Plasma Theory General stability theory in plasma physics*. Academic Press, p. 54
- Kunz M. W., Schekochihin A. A., Stone J. M., 2014, *Physical Review Letters*, 112, 205003
- Lyutikov M., 2006, *MNRAS*, 373, 73
- Markevitch M., Ponman T. J., Nulsen P. E. J., Bautz M. W., Burke D. J., David L. P., Davis 2000, *ApJ*, 541, 542
- Markevitch M., Vikhlinin A., 2007, *Phys. Rep.*, 443, 1
- Melville S., Schekochihin A. A., Kunz M. W., 2015, *ArXiv: 1512.08131*
- Pal'chikov V. G., Shevelko V. P., 1995, *Reference Data on Multicharged Ions*. Vol. 16, Springer-Verlag Berlin Heidelberg New York
- Parker E. N., 1958, *Phys. Rev.*, 109, 1874
- Riquelme M., Quataert E., Verscharen D., 2016, *ArXiv: 1602.03126*
- Sazonov S. Y., Churazov E. M., Sunyaev R. A., 2002, *MNRAS*, 333, 191
- Sazonov S. Y., Sunyaev R. A., 1999, *MNRAS*, 310, 765
- Schekochihin A. A., Cowley S. C., 2006, *Phys. Plasmas*, 13, 056501
- Schekochihin A. A., Cowley S. C., Rincon F., Rosin M. S., 2010, *MNRAS*, 405, 291
- Schuecker P., Finoguenov A., Miniati F., Böhringer H., Briel U. G., 2004, *A&A*, 426, 387
- Sharma P., Hammett G. W., 2011, *J. Comp. Phys.*, 230, 4899
- Sharma P., Hammett G. W., Quataert E., Stone J. M., 2006, *ApJ*, 637, 952
- Soffitta P., Barcons X., Bellazzini R., Braga J., Costa E., Fraser G. W., Gburek S., Huovelin J., Matt G., Pearce M., Poutanen J., Reglero V., Santangelo A., Sunyaev R. A., Tagliaferri G., 2013, *Experimental Astronomy*, 36, 523
- Spitzer L., 1962, *Physics of Fully Ionized Gases*. New York: Interscience
- Stone J. M., Gardiner T., 2009, *New A*, 14, 139
- Subramanian K., Shukurov A., Haugen N. E. L., 2006, *MNRAS*, 366, 1437
- Sunyaev R. A., Zeldovich I. B., 1980, *MNRAS*, 190, 413
- Vikhlinin A., Markevitch M., Murray S. S., 2001, *ApJ*, 549, L47
- Vikhlinin A. A., Markevitch M. L., 2002, *Astron. Lett.*, 28, 495

Vogt C., Enßlin T. A., 2005, *A&A*, 434, 67

Weisskopf M. C., Baldini L., Bellazini R., Brez A., Costa E., Dissly R., Elsner R. F., Fabiani S., Matt G., Minuti M., Muleri F., O'Dell S., Pinchera M., Ramsey B., Rubini A., Sgro' C., Soffitta P., Spandre G., 2013, in *UV, X-Ray, and Gamma-Ray Space Instrumentation for Astronomy XVIII* Vol. 8859 of Proc. SPIE, A small mission featuring an imaging x-ray polarimeter with high sensitivity. p. 885908

Weisskopf M. C., Silver E. H., Kestenbaum H. L., Long K. S., Novick R., 1978, *ApJ*, 220, L117

Zhuravleva I., Churazov E., Schekochihin A. A., Allen S. W., Arévalo P., Fabian A. C., Forman W. R., Sanders J. S., Simionescu A., Sunyaev R., Vikhlinin A., Werner N., 2014, *Nature*, 515, 85

Zhuravleva I. V., Churazov E. M., Sazonov S. Y., Sunyaev R. A., Forman W., Dolag K., 2010, *MNRAS*, 403, 129

## APPENDIX A: TOTAL ANISOTROPY AND MICROSCALE INSTABILITIES

Here, for illustrative purposes, we calculate the total anisotropy  $\Delta_e + \Delta_i$  by equation (10) for the two simulated cold fronts with homogeneous and random magnetic fields. As it is seen in Fig. A1, the ion contribution to the anisotropy is large enough to trigger the firehose and mirror instabilities all over the computational domain. The plasma is rendered unstable when  $|\Delta_e + \Delta_i| \gtrsim 1/\beta$ . The instabilities maintain the plasma in the marginal state:  $\Delta_e + \Delta_i \approx 1/\beta$  for the mirror (the general mirror instability condition reduces to this simple expression when both the ion and electron anisotropies are small:  $\Delta_e \ll 1$ ,  $\Delta_i \ll 1$ ),  $\Delta_e + \Delta_i = -2/\beta$  for the firehose instabilities. In some regions,  $\beta$  becomes low and allows a rather high level of anisotropy, while keeping the plasma stable. In the case of a homogeneous magnetic field, this is clearly seen in the low- $\beta$  layer around the cold front and behind the front, where the magnetic field is amplified by turbulent eddies. In the case of a random magnetic field, stable regions of high anisotropy form behind the front.

## APPENDIX B: RELATIVISTIC BREMSSTRAHLUNG DIFFERENTIAL CROSS SECTIONS

The expressions for the relativistic bremsstrahlung differential cross sections were first given by Gluckstern & Hull (1953). After being rearranged in a more convenient way (Bai & Ramaty 1978) and corrected for typos, they read

$$d^2\sigma_{\perp} = A \left( B_{\perp} + \frac{L}{pp'} C_{\perp} + \frac{l_0}{p'Q} D_{\perp} - \frac{E}{p^2 \sin^2 \theta} \right), \quad (\text{B1})$$

$$d^2\sigma_{\parallel} = A \left( \tilde{B}_{\parallel}(\theta) + \frac{L}{pp'} \tilde{C}_{\parallel}(\theta) + \frac{l_0}{p'Q} D_{\parallel} + \frac{E}{p^2 \sin^2 \theta} \right), \quad (\text{B2})$$

$$A = \frac{Z^2 r_0^2 p' 1}{8\pi 137 p \epsilon}, \quad (\text{B3})$$

$$B_{\perp} = -\frac{5\gamma^2 + 2\gamma\gamma' + 1}{p^2\delta^2} - \frac{p^2 - k^2}{Q^2\delta^2} - \frac{2k}{p^2\delta}, \quad (\text{B4})$$

$$B_{\parallel} = -\frac{5\gamma^2 + 2\gamma\gamma' + 5}{p^2\delta^2} - \frac{p^2 - k^2}{Q^2\delta^2} + \frac{2(\gamma + \gamma')}{p^2\delta} - \frac{4l}{p'\delta}, \quad (\text{B5})$$

$$\tilde{B}_{\parallel}(\theta) = B_{\parallel} + \frac{8(2\gamma^2 + 1)}{p^2\delta^4} \sin^2 \theta, \quad (\text{B6})$$

$$C_{\perp} = \frac{2\gamma^2(\gamma^2 + \gamma'^2) - (5\gamma^2 - 2\gamma\gamma' + \gamma'^2)}{p^2\delta^2} + \frac{k(\gamma^2 + \gamma\gamma' - 2)}{p^2\delta}, \quad (\text{B7})$$

$$C_{\parallel} = \frac{2\gamma^2(\gamma^2 + \gamma'^2) - (9\gamma^2 - 4\gamma\gamma' + \gamma'^2) + 2}{p^2\delta^2} + \frac{k(\gamma^2 + \gamma\gamma')}{p^2\delta}, \quad (\text{B8})$$

$$\tilde{C}_{\parallel}(\theta) = C_{\parallel} + \frac{4\gamma(3k - p^2\gamma')}{p^2\delta^4} \sin^2 \theta, \quad (\text{B9})$$

$$D_{\perp} = \frac{k}{\delta} - \frac{k(p^2 - k^2)}{Q^2\delta} + 4, \quad (\text{B10})$$

$$D_{\parallel} = \frac{4}{\delta^2} - \frac{7k}{\delta} - \frac{k(p^2 - k^2)}{Q^2\delta} - 4, \quad (\text{B11})$$

$$E = \frac{2L}{pp'} \left( 2\gamma^2 - \gamma\gamma' - 1 - \frac{k}{\delta} \right) - \frac{4l_0}{p'Q} (\delta - \gamma')^2 - \frac{2l(\delta - \gamma')}{p'}, \quad (\text{B12})$$

where

$$\gamma = E/m_e c^2 + 1; \quad \gamma' = \gamma - \epsilon/m_e c^2; \quad (\text{B13})$$

$$p = \sqrt{\gamma^2 - 1}; \quad p' = \sqrt{\gamma'^2 - 1}; \quad k = \epsilon/m_e c^2; \quad (\text{B14})$$

$$Q^2 = p^2 + k^2 - 2pk \cos \theta; \quad \delta = \gamma - p \cos \theta; \quad (\text{B15})$$

$$L = 2 \ln \left( \frac{\gamma\gamma' + pp' - 1}{\gamma\gamma' - pp' - 1} \right); \quad l = \ln \left( \frac{\gamma' + p'}{\gamma' - p'} \right);$$

$$l_0 = \ln \left( \frac{Q + p'}{Q - p'} \right); \quad (\text{B16})$$

$r_0 = e^2/(m_e c^2) \approx 2.82 \times 10^{-13}$  cm is the classical electron radius, the rest of the notations were introduced in Section 2.2.

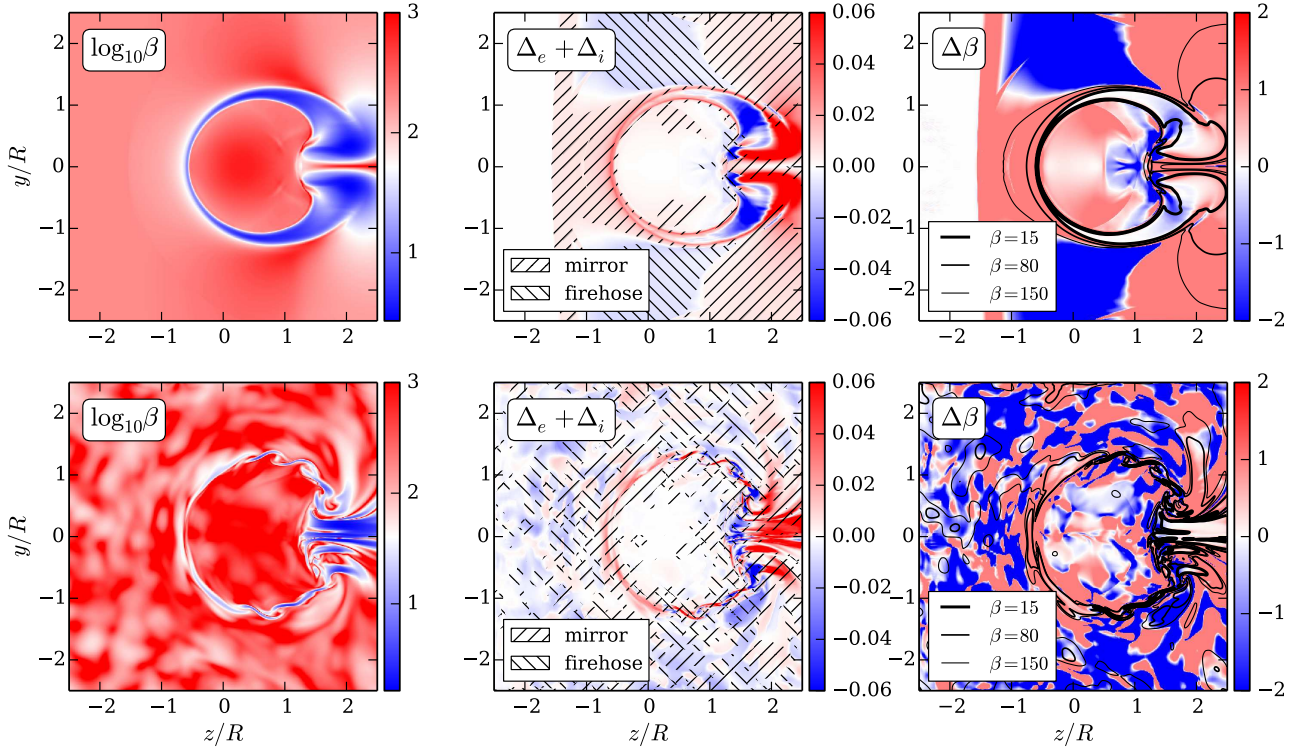


**Figure A1.** The total (ion+electron) anisotropy for the simulated cold fronts. *Left panels:* the plasma  $\beta$ . *Middle panels:* the total anisotropy  $\Delta_e + \Delta_i$ , unstable regions are hatched; in the unstable regions, the plasma is kept marginal:  $\Delta_e + \Delta_i \approx 1/\beta$  for the mirror,  $\Delta_e + \Delta_i = -2/\beta$  for the firehose instabilities. *Right panels:* the total anisotropy multiplied by  $\beta$  with contours of  $\beta$  overlaid; this quantity is equal to 1 in the mirror-unstable regions, and -2 in the firehose-unstable regions.